Aerodynamic interaction of side-by-side propellers in forward flight operating at low-Reynolds numbers

Original
Aerodynamic interaction of side-by-side propellers in forward flight operating at low-Reynolds numbers / Comunian, P., Montagner, S., Serpieri, J., Cafiero, G.. - In: AEROSPACE SCIENCE AND TECHNOLOGY. - ISSN 1270-9638. - 171:(2026). [10.1016/j.ast.2025.111577]

Publisher:
Elsevier

Published
DOI:10.1016/j.ast.2025.111577

Aerospace Science and Technology 171 (2026) 111577

Contents lists available at ScienceDirect

Aerospace Science and Technology

journal homepage: www.elsevier.com/locate/aescte

Original article

Aerodynamic interaction of side-by-side propellers in forward flight operating at low-Reynolds numbers

Paolo Comunian *, Sara Montagner, Jacopo Serpieri, Gioacchino Cafiero

Department of Mechanical and Aerospace Engineering, Politecnico di Torino, Corso Duca degli Abruzzi 24, Turin, 10129, Italy

ARTICLE INFO

Communicated by Dr. Tianxiang Hu

PACS:
0000
1111

2000 MSC:
0000
1111

Keywords:
Low-reynolds number propellers
Propeller interaction
SPIV

ABSTRACT

An experimental investigation is conducted to study the interaction of side-by-side propellers operating in forward flight at low Reynolds numbers. The effect on performance is first evaluated by means of load cell measurements, while the flow field is studied employing a stereoscopic particle image velocimetry (SPIV) setup. Three different configurations are tested: single propeller, co-rotating and counter-rotating cases at varying advance ratios. The results indicate that the performance of the single propeller is decreased due to aerodynamic interaction, leading to an average 3.2% reduction in propulsive efficiency, evaluated across all the tested operating conditions. The effect is stronger at lower advance ratios, owing to a greater interaction between the two streamtubes in such conditions. SPIV measurements indicate a widening of the wake as well as a reduction in the turbulence intensity for the cases with two propellers, with a stochastic fluctuations approximately 15% lower for the twin propeller cases than the single propeller. The data is then sorted and phase-ordered a posteriori via a data-driven approach, effectively reconstructing phase-averaged flow fields. This enables the decomposition of the velocity field into phase-correlated and purely turbulent components. The results show that the stochastic (turbulent) component of the velocity field increases when the propellers operate at advance ratios different from the maximum efficiency condition.

1. Introduction

Current advancements in electric-powered air mobility systems have increased the interest in propeller aerodynamics. New urban air mobility concepts like eVTOLs, UAV technology, and disruptive designs for future electrically powered aircraft all feature propellers as their propulsion device. It is often the case that these designs see propellers positioned in close proximity, as it is the case for distributed electric propulsion (DEP) [1–3] or small UAVs featuring tandem propellers [4], for instance. In this context, a proper understanding of the interaction mechanisms becomes fundamental, as they lead to changes in propeller performance, as well as to the structure of the flow field.

Small UAVs operate at low Reynolds numbers [5]. Due to their size and operating condition, the propeller's blade chord-based *Re* number is often below 10^5.

This flow regime poses several challenges owing to the complex flow field that characterizes the pressure and suction side of the blades. Indeed, numerous investigations [6,7] have shown the formation of a laminar separation bubble at values of the blade tip Reynolds number ranging from $4.3 \cdot 10^4$ to $5 \cdot 10^5$. In this regime, laminar to turbulent transition is highly affected by the inflow conditions, leading to an effect on performance and also on noise generation [7]. In this regard, inflow turbulence can play a role as it affects the boundary layer transition and, consequently, the propeller performance and noise [8]. The numerical analysis of the flow field is also quite challenging, owing to the limited value of the Reynolds number. Low-order approaches, such as the VPM (Vortex Particle Method), rely on the computation of the airfoil polars [9], which can be cumbersome. On the other hand, higher fidelity methods can be prohibitive owing to the computational cost.

Unlike the case of turboprops or helicopter blades, small propellers usually have a fixed blade pitch angle. This implies that a variation in thrust requires a variation in rotational speed, and that the propeller disk must be tilted to perform any kind of maneuver. As a consequence, propellers are likely to encounter a non-axial inflow condition [10]. These considerations are also relevant for adjacent propellers, as they also lead to non-uniform inflow conditions [1]. This can be important when considering the blade loading, as non-uniform inflow conditions also lead to an unsteady blade loading [11].

The aerodynamic interaction between side-by-side propellers can be subdivided into three major effects. Firstly, a reduction in propeller performance has been observed in the twin propellers case [12]. Previous works [13] found a maximum 2% reduction in thrust coefficient for a minimum separation distance of 0.05 D, where D indicates the propeller diameter, while in [14] a 6.3% reduction in thrust is indicated.

---

[*] Corresponding author.

https://doi.org/10.1016/j.ast.2025.111577
Received 23 July 2025; Received in revised form 21 November 2025; Accepted 24 December 2025
Available online 8 January 2026

Nomenclature

CCW = counter clock-wise
CW = clock-wise
CoR = co-rotating
CnR = counter-rotating
BPF = blade passing frequency [Hz]
T = thrust [N]
Q = torque [Nm]
η = efficiency
D = propeller diameter [m]
R = propeller radius [m]
V = velocity magnitude [m/s]
n = rotational speed [1/s]
C_τ = thrust coefficient $T/(\rho n^2 D^4)$
C_Q = torque coefficient $Q/(\rho n^2 D^5)$
J = advance ratio $V/(nD)$
RPM = revolutions per minute
u, v, w = velocity components [m/s]
Re = Reynolds Number $\frac{Vc}{\nu}$
ρ = air density [kg/m^3]
ν = kinematic viscosity [m^2/s]
TKE = turbulent kinetic energy [m^2/s^2]
PKE = phase-correlated kinetic energy [m^2/s^2]
$_\infty$ = free stream conditions
$_{tip}$ = blade tip

Additionally, a 1.5% reduction in efficiency is reported in [1], finding no significant differences between a counter-rotating and a co-rotating configuration. Secondly, a modification of the flow field structure is expected, as the slipstreams interact and evolve differently from the isolated case. In [15], an induced upwash is observed between the propellers in the counter-rotating case. The interaction between propellers also leads to an uneven loading on the propeller disk [1,16], associated with higher fluctuations in the measured thrust [13], which increases as the separation between propellers is reduced. Lastly, an increase in noise production is also expected. Several studies [1,17–19] have investigated the effect of the different relative phases between propeller blades, suggesting that there is an effect on the directionality of the emitted noise and on the tonal contribution, while no significant effects were found on the broadband noise, on the performance, or on the structure of the time-averaged flow field.

Most of the experimental work found in the literature about the aerodynamic interaction of side-by-side propellers focuses on the hovering condition (e.g. [4,13]), while less attention has been paid to the forward flight cases [1], investigating the effect of different advance ratios. The primary objectives of this work are to assess the effects on performance of small adjacent propellers at different advance ratios when operating at low Reynolds number and to study how the slipstream is modified due to aerodynamic interaction. The investigation focuses on the condition corresponding to the maximum interaction between the two propellers, namely when the tip-to-tip clearance is reduced to a minimum. Firstly, their performance is measured for a range of operating conditions, covering the full envelope of advance ratios that produce thrust for the chosen propeller. This is done both in a co- and a counter-rotating configuration. Subsequently, the slipstream structure is studied through low-speed stereoscopic particle image velocimetry for three representative advance ratios, comparing a single propeller with two co-rotating (CoR) and counter-rotating (CnR) propellers.

In the current manuscript, the analysis focuses on the conditions that yield the greatest interaction between two propellers operating in close proximity. Besides providing confirmation for the already evidenced mechanism of thrust reduction, also at low values of the Reynolds number, the study aims at clarifying the effects of the interaction on the turbulence in the slipstream.

Using the methodology presented in Amico et al. [20], a surrogate of the temporal evolution of the wake is obtained. With this, a triple decomposition of the velocity field is performed, allowing to separate between the contributions associated with the periodic forcing and the actual stochastic content in the slipstream.

2. Experiment design

The experiments were conducted in the Ferrari Wind Tunnel, an open-jet facility at the Politecnico di Torino. The tunnel is constituted by a contraction with a contraction ratio of 3.5 : 1, with an exit diameter of 0.45 m. The test section is a cubic enclosure with side 0.9 m, which then culminates into a conical divergent, with a diffusing ratio of 1 : 2.4. The fan is located at the end of the divergent section and allows a range of stable flow speeds in the test section between 1 and 20 m/s. The flow quality was characterised with an empty test section at different speeds, showing turbulence intensity levels of 0.8% [10]. The overview of the experimental setup is shown in Fig. 1.a,b. Each propeller has a radius (R) equal to 0.15 m and it was mounted in a tractor configuration, on a dedicated support which was 3D printed in PLA (polylactic acid), ensuring that their axes of rotation were parallel to each other, with a center-to-center distance of 0.16 m (i.e. 2.13R), leading to a tip-to-tip distance between the two propellers of 0.01 m. Previous studies [13,14,21] show that minimizing the tip-to-tip spacing between propellers operating in side-by-side arrangement leads to the strongest interaction in both in the slipstream modification and in the decreased performance. The tip-to-tip distance of 0.01 m was chosen to be the minimum distance allowing the safe operation of the propellers, accounting for vibrations or deflections of the blade. The propellers were placed at 1 R from the inlet of the test section, with their axes aligned with the freestream, namely in a forward flight configuration. As a result, the disk area of a single propeller corresponds to approximately 11% of the wind tunnel nozzle exit area, increasing to about 22% when both propellers are operated simultaneously.

The supports of the two propellers have identical external geometries to minimize the asymmetries in the flow. However, they differ in functionality: one of the supports is equipped with a load cell and a torque cell, while the other is designed to replicate the same geometric dimensions but contains only mock versions of the cells. This is done to avoid any bias in the measurements due to the different supports of the propellers. The supports extend along the propeller axis such that the torque cell is 2.76 R downstream the propeller, as seen in Fig. 1.a, again to minimize the impact on the flow development.

The propellers were 3D printed in VisiJet M2R-CL resin. Their geometry, shown in Fig. 3, is the same used in [10], resulting in a range of Reynolds numbers based on the chord at 75% of R between $1 \cdot 10^4$ and $3 \cdot 10^4$. The blade design is derived from a two-bladed APC 9×6 model, reshaped using a NACA 4412 airfoil, as described in detail by Casalino et al. [7]. The reason for adopting this geometry is that it allows a straightforward numerical reproduction of the same blade. This propeller was indeed chosen as several experimental and numerical studies are found in the literature featuring the same geometry. Applications are found in experimental acoustics [7,8,22,23], numerical acoustics [24–26], and in the investigation of non-uniform inflow conditions [9,27].

Each propeller is driven by a RCS-TRX 370 2826 1000KV brushless direct current (BLDC) motor with a diameter of 2.8 cm and a maximum rated power of 150 W. Each motor is controlled by an external electronic speed controller (ESC) that receives input commands from an Arduino Uno board. The rotational speed (expressed in revolutions per minute, RPM) of each motor is individually managed by a Proportional-Integrative-Derivative (PID) controller. The RPM feedback signal is measured for each motor using a Hobbywing RPM sensor, connected to two of the three phases of the respective brushless motor. For each revolution, the sensor records seven peaks corresponding to the commutation

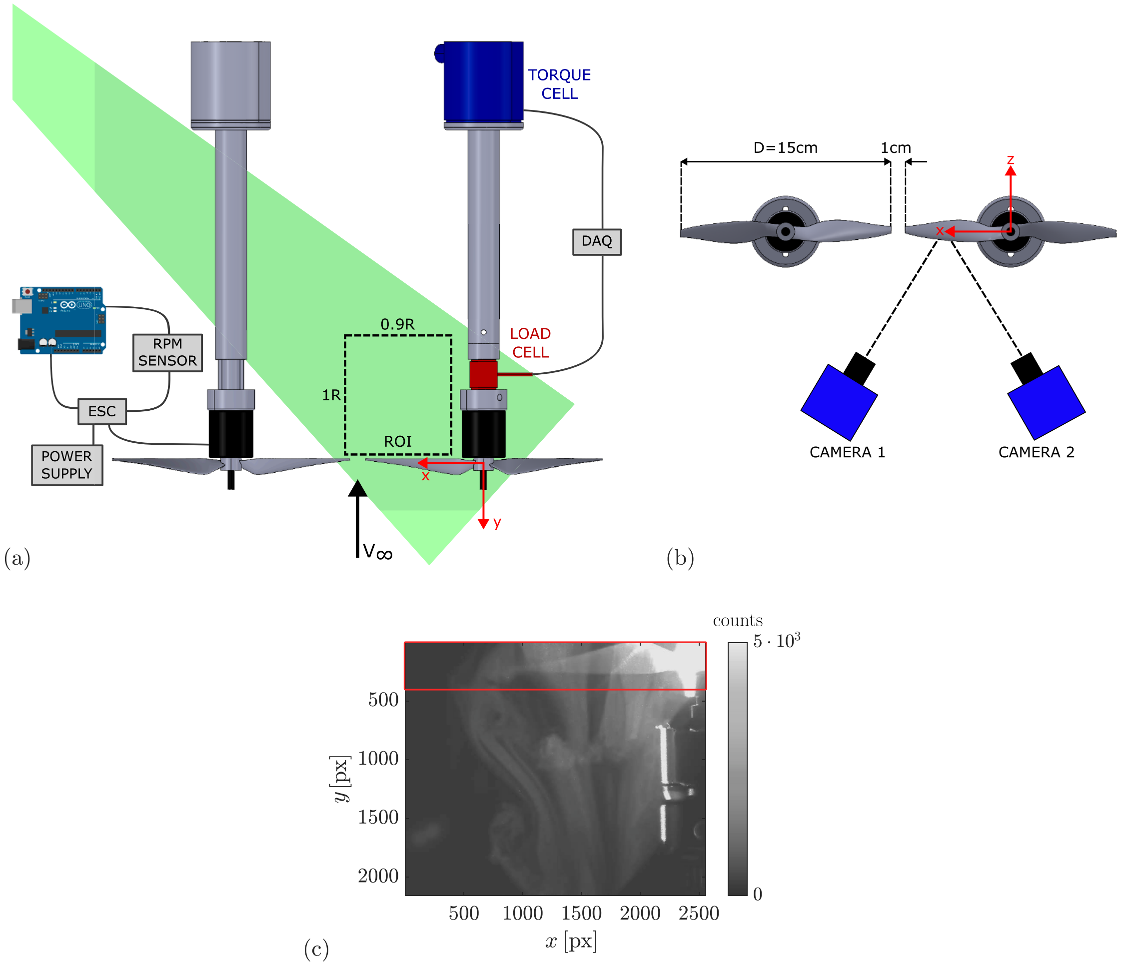

Fig. 1. Schematic of the experimental setup and its main components: (a) top view and (b) front view. The strut on the left is equipped with a rectangular opening that enables the laser sheet to illuminate the measurement plane. (c) Example of a raw camera image. The region highlighted in red marks the portion of the image in which the blade appears in different positions; this region is used to implement the ISOMAP algorithm and perform the phase recognition.. (For interpretation of the references to colour in this figure legend, the reader is referred to the web version of this article.)

Table 1
Load and torque cells parameters.

Load cell futek LSB201		Torque cell futek TFF400	
Rated Output (RO)	250 g	Rated Output (RO)	0.07 N m
Excitation	5 V	Excitation	10 V
Nonlinearity	± 0.1% of RO	Nonlinearity	± 0.2% of RO
Hysteresis	± 0.1% of RO	Hysteresis	± 0.2% of RO
Nonrepeatability	± 0.05% of RO	Nonrepeatability	± 0.05% of RO
RSS error	± 0.15% of RO	RSS error	± 0.28% of RO

of the motor's magnetic poles, and they are then used to evaluate the RPM. The standard deviation of the measured RPM averaged across all cases was within 2% of the target value.

2.1. Thrust and torque measurements

The system used for force and torque measurements consists of a FUTEK LSB201 axial load cell and a FUTEK TFF400 torque cell. Table 1 summarizes the specifications of the sensors. The data were recorded for 45 seconds using a National Instrument 9215 module at a frequency of 5 kHz.

To assess the effect of the aerodynamic interaction on performance, the thrust and the torque were measured at different advance ratios ($J = V_\infty/(nD)$) ranging from 0 to 0.7. This was achieved by a combination of freestream velocities (V_∞) and rotational speeds (RPM), ranging from 1 m/s to 9 m/s and 1500 RPM to 7000 RPM, respectively.

For each combination of RPM and V_∞, four cases were evaluated: one counter-clockwise (CCW) propeller, one clockwise (CW) propeller, two counter-rotating propellers, and two co-rotating propellers (see Fig. 2.a,b). The cases with one propeller are used as a reference. The CnR and CoR configurations were obtained by switching the propeller mounted on the support equipped with the load measurement system; the other propeller was always a CCW one. To ensure statistical convergence, each measurement lasted 45 s. Moreover, every test case was repeated three times to ensure repeatability.

2.2. Flow field measurements

A stereoscopic particle image velocimetry (SPIV) [28,29] setup was employed to study the flow field. The illumination of the region of interest was ensured by a Litron Nano PIV Series Nd:YAG Dual Power laser with 200 mJ/pulse energy, operating at 15 Hz in dual pulse mode. The laser beam was shaped into a sheet with a thickness of about 1 mm using a spherical lens with focal length of 1000 mm and a cylindrical lens with focal length of −50 mm.

Two Andor Zyla 5.5 MP sCMOS cameras, with sensor size of 2560 × 2160 pixels^2 and with pixel size of 6.5 μm), each equipped with a Tokina ATX-I macro lenses with 100 mm focal length operated at a value of the aperture of $f_\# = 11$ and $f_\# = 5.6$, were employed to collect im-

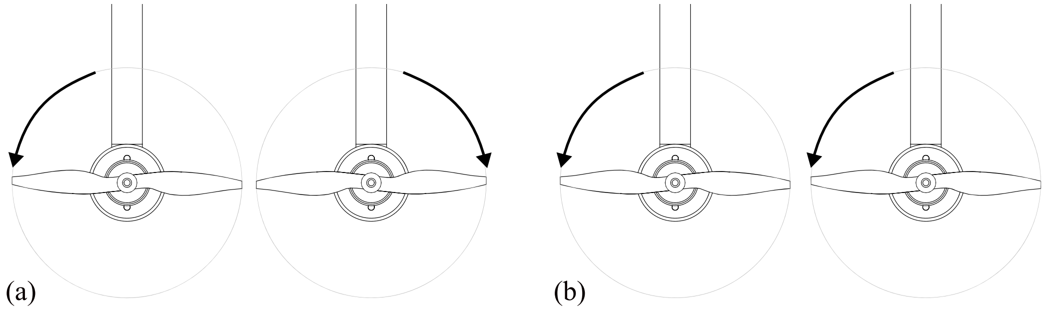

Fig. 2. Schematic (front view) of the considered setup: (a) Counter-rotating configuration. (b) Co-rotating configuration..

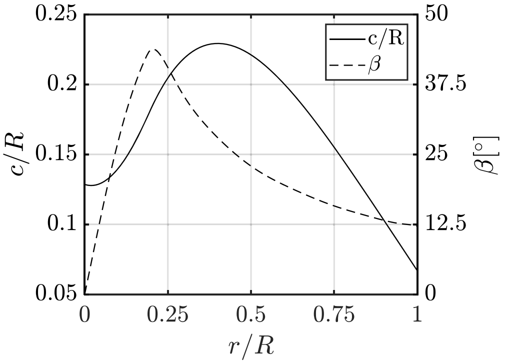

Fig. 3. Blade chord and pitch angle distributions.

ages of the tracer particles. The two different values of the aperture were chosen to minimize the differences in the illumination of the two cameras, arranged in forward and backward scatter configuration, leading to an angle between the cameras of about 50 degrees. Each camera was equipped with a Scheimpflug adapter to guarantee uniform focusing across the entire image. The cameras and the laser were synchronized and driven by a PCI 6602 counter. The time interval between the laser pulses was set to 60 µs or 80 µs depending on the propeller operating condition, and was chosen to have a displacement between two frames of approximately 12 pixels.

The region of interest (ROI), indicated in Fig. 1, extends for 0.9 R along the streamwise direction and 1 R in the plane containing both propellers' rotation axis, corresponding to a digital resolution of 30 px/mm. The ROI is positioned downstream the propeller mounted on the instrumented support, i.e. the one equipped with the load and torque cells (see Fig. 1.a).

For each investigated case, three advance ratios were considered to analyze different operating conditions of the considered propeller: hovering ($J = 0$), maximum efficiency ($J = 0.45$), and a third point representing a high loading case in forward flight ($J = 0.3$). All the test cases considered are summarized in Table 2, corresponding to a single CCW propeller (from now on indicated as CCW in the Figures), two co-rotating propellers, and two counter-rotating propellers.

For each case, 800 instantaneous image pairs were recorded. The camera calibration was performed using the pin-hole model [30], with a residual calibration error of about 0.6 pixels. A self-calibration, implemented according to the algorithm proposed by Wieneke [31], allowed to further reduce the error below 0.1 pixel [32].

In the raw images of the tracer particles, the blade of one propeller is visible as it passes through the camera's field of view, as shown in Fig. 1.c. This generates reflections that must be removed to improve the accuracy of the image processing phase. To accomplish this, a pre-processing of the raw images was carried out, using the anisotropic diffusion method proposed by Adatrao and Sciacchitano [33]. This method enhances image quality by reducing noise while preserving sharp edges, generating two outputs: a clean image, free of unwanted reflections for accurate PIV processing, and a background image, where the reflections produced by the blade are isolated.

The correlation on the pre-processed images was then performed using a multi-step algorithm with a final interrogation size of 32×32 pixels^2 (i.e., about $1.06 \times 1.06\,\mathrm{mm}^2$) with 75% overlap, resulting in about 56 vectors per diameter (D). The uncertainty in the displacement of the particle pixels is ±0.8% and ±5%, respectively, for the two in-plane components and the out-of-plane component. The entire processing, including geometric calibration, self-calibration and correlation, was carried out using PaIRS [34], freely downloadable at: https://www.pairs.unina.it/.

2.3. Phase-resolved analysis and decomposition of velocity components

The background images, obtained through the anisotropic diffusion method [33], play a crucial role in the phase-recognition process, as they provide a reliable way to track the blade's position across different snapshots. It should be noted that these background images are extracted from the raw camera acquisitions, which cover a wider field of view than the final SPIV region of interest. In this wider field, part of the blade is always visible as it crosses the camera's view, enabling its position to be tracked for phase recognition, as illustrated in Fig. 1.c. Since the experimental setup does not include an encoder to measure the angular position of the propeller, an a posteriori phase-recognition approach was implemented. Following the method proposed by Amico et al. [20], the background images were used as input to an ISOMAP-based algorithm to reorder the image pairs according to the blade's position. ISOMAP is a nonlinear dimensionality reduction technique that maps high-dimensional data onto a low-dimensional space while preserving the distance between images [35]. The images were ordered based on their proximity in the reduced-dimensional space, where image pairs

Table 2
Flow field SPIV test conditions for three configurations: isolated propeller CCW, two propellers CoR and two propellers CnR..

case	A2	A4	A5	S1	S2	S3	S4	S5	S6
J		0			0.3			0.45	
RPM	3000	5000	6000	3000	5000	6000	3000	5000	6000
V_∞ [m/s]	0	0	0	2.25	3.75	4.5	3.4	5.6	6.75
$Re_{0.75} \cdot 10^{-3}$	13.3	22.1	26.6	13.4	22.3	26.8	13.5	22.6	27.1

with similar blade positions naturally cluster along a continuous trajectory. This sorting process enables an unsupervised phase-recognition process by leveraging the spatial coherence of the blade's motion.

Once the image pairs were correctly ordered in phase, phase-averaged velocity fields were computed by dividing the images into 25 equal-sized subsets, each corresponding to a specific interval along the ISOMAP trajectory. The choice of $N_{\text{phases}} = 25$ was a trade-off between achieving a fine phase resolution and ensuring a sufficient number of image pairs per subset to reduce both the random measurement noise and the phase-uncorrelated signal. In the present study, the propeller has two blades, the blade passing frequency identifies an angle of 180°; therefore, 25 phase intervals are used to discretize the 180° rotation. Each angular bin corresponds to 7.2°. The phase-averaged fields are obtained by averaging all the instantaneous velocity fields within ±3.6° from the center of each interval. A convergence analysis was performed to assess the reliability of the phase-averaging process. The evaluation focused on a central portion of the wake, extending approximately $0.35R$ in the radial direction (x) and $0.7R$ in the streamwise direction (y), while excluding the outer regions, which are more affected by spurious reflection. For each phase f, $N = 32$ instantaneous velocity fields ($u_i(\mathbf{x})$) were available, and the statistical convergence within the selected region was assessed as follows. The phase-averaged velocity field was first obtained as:

$$\mu_f(\mathbf{x}) = \frac{1}{N}\sum_{i=1}^{N} u_i(\mathbf{x}). \tag{1}$$

Then, the corresponding standard deviation of the ensemble was evaluated as:

$$\sigma_f(\mathbf{x}) = \sqrt{\frac{1}{N-1}\sum_{i=1}^{N}\left(u_i(\mathbf{x}) - \mu_f(\mathbf{x})\right)^2}. \tag{2}$$

The coefficient of variation for each phase CV_f was then obtained as the spatial average over the selected region of the ratio $\sigma_f(\mathbf{x})/\mu_f(\mathbf{x})$, multiplied by 100. In other words, CV_f is a scalar value representing the mean percentage fluctuation of the instantaneous velocity fields with respect to their phase average. Finally, a global convergence metric was defined as the average of CV_f across all the 25 phases:

$$CV = \frac{1}{N_{\text{phases}}}\sum_{f=1}^{N_{\text{phases}}} CV_f. \tag{3}$$

In the worst operating condition the CV is about 5.7%, with a maximum CV_f of 6.3%, while in the best case the corresponding values decrease to 1.7% and 1.9%, respectively.

With the image pairs sorted in phase, the velocity field was analyzed using a decomposition approach to separate different contributions to the flow dynamics. The triple decomposition [36,37] was deployed:

$$\mathbf{u}(\mathbf{x},t) = \overline{\mathbf{u}}(\mathbf{x}) + \tilde{\mathbf{u}}(\mathbf{x},t) + \mathbf{u}''(\mathbf{x},t) \tag{4}$$

where $\mathbf{u}(\mathbf{x},t)$ is the full velocity field, $\overline{\mathbf{u}}(\mathbf{x})$ represents the time-averaged velocity, $\tilde{\mathbf{u}}(\mathbf{x},t)$ is the phase-correlated organized contribution to the velocity fluctuations, and $\mathbf{u}''(\mathbf{x},t)$ accounts for the stochastic, non-coherent fluctuations. The phase-correlated component is obtained as:

$$\tilde{\mathbf{u}}(\mathbf{x},t) = \langle \mathbf{u}(\mathbf{x},t)\rangle - \overline{\mathbf{u}}(\mathbf{x}) \tag{5}$$

where $\langle \mathbf{u}(\mathbf{x},t)\rangle$ represents the phase-averaged velocity field according to the characteristic period τ:

$$\langle \mathbf{u}(\mathbf{x},t)\rangle = \lim_{N\to\infty}\frac{1}{N}\sum_{n=1}^{N}\mathbf{u}(\mathbf{x},t+n\tau) \tag{6}$$

Even with the PID controller, keeping the value of the RPM of the propeller at stable values for a very long time is not trivial. Therefore, a direct application of Eq. (6) is not advisable. Leveraging the phase-recognition method described earlier, it was possible to reorder the sequence of image pairs and obtain a statistically robust phase-averaged velocity field [20].

A useful way to quantify the effects of periodic forcing and turbulence in the flow is through the analysis of kinetic energy components. The total kinetic energy can be decomposed into three contributions: the mean kinetic energy (MKE), the turbulent kinetic energy (TKE), and the phase-correlated kinetic energy (PKE). The TKE represents the energy associated with stochastic turbulent fluctuations and is defined as:

$$TKE(\mathbf{x}) = \sum_{i=1}^{3}\left[\lim_{T\to\infty}\frac{1}{T}\int_0^T u_i''^2(\mathbf{x},t)\,dt\right] \tag{7}$$

Conversely, the PKE quantifies the energy contained in the organized, phase-correlated motions induced by the periodic blade passage and is given by:

$$PKE(\mathbf{x}) = \sum_{i=1}^{3}\left[\lim_{T\to\infty}\frac{1}{T}\int_0^T \tilde{u}_i^2(\mathbf{x},t)\,dt\right] \tag{8}$$

The spatial distribution of PKE and TKE allows us to infer how much of the flow dynamics is dominated by the periodic motion of the propeller and how much is driven by stochastic turbulence. This approach not only improves the quality of the PIV analysis, but also provides a more detailed understanding of the periodic flow structures induced by the propeller motion, distinguishing them from random turbulent fluctuations.

Effect on the propeller slipstream's pitch

Propeller-wing interaction is fundamental for wing-mounted propellers. In Sinnige et al. [38], the ratio between the average distance between two successive tip vortices, usually labelled pitch, and the wing's chord length is highlighted as an important factor related to the unsteady loading of a lifting surface. In this regard, knowing whether there is an effect due to the interacting propellers becomes relevant.

To obtain an estimate of the average distance between two consecutive tip vortices, the z-component of the vorticity fluctuation ($\Omega_z'(\mathbf{x},t)$), obtained through the Reynolds decomposition, was sampled along the maximum time-averaged vorticity line, $\mathbf{s}$, in Fig. 4.a. In most of the snapshots, at least two tip vortices are captured; this allows to perform an auto-correlation (Eq. (9)) of the sampled signal along the line $\mathbf{s}$ (Fig. 4.b),

$$\lambda(\Delta\mathbf{s}) = \int_0^\infty f(\mathbf{s})(\mathbf{s}+\Delta\mathbf{s})d\mathbf{s} \tag{9}$$

and attribute the spatial separation distance with the correlation peak to the distance between the two vortical structures (Fig. 4.c). Subsequently, a distribution is constructed (Fig. 4.d) excluding the cases corresponding to snapshots where only one tip vortex was captured. Lastly, the mean is taken, obtaining a single value for the pitch for each of the cases in Table 2. It is worth noting that the pitch identified with this approach represents its value, divided by the number of blades.

3. Results

3.1. *Propellers performance*

Considering the blade geometry indicated in Fig. 3, a CW or CCW propeller should produce the same thrust and torque at a given operating condition. The only difference should be the sign of the torque. Before delving into the detailed description of the interaction under different operating conditions, the thrust, torque and efficiency values were measured for a range of operating conditions for both the CW and CCW propellers, as indicated in Section 2. The efficiency ($\eta = TV_\infty/(2\pi nQ)$) measured for the CW and CCW propellers is reported in Fig. 5. The results show no significant differences between the CW and CCW propellers, as it was expected. The errorbars in Fig. 5 represent the estimated uncertainty in the measurement of the propeller efficiency due

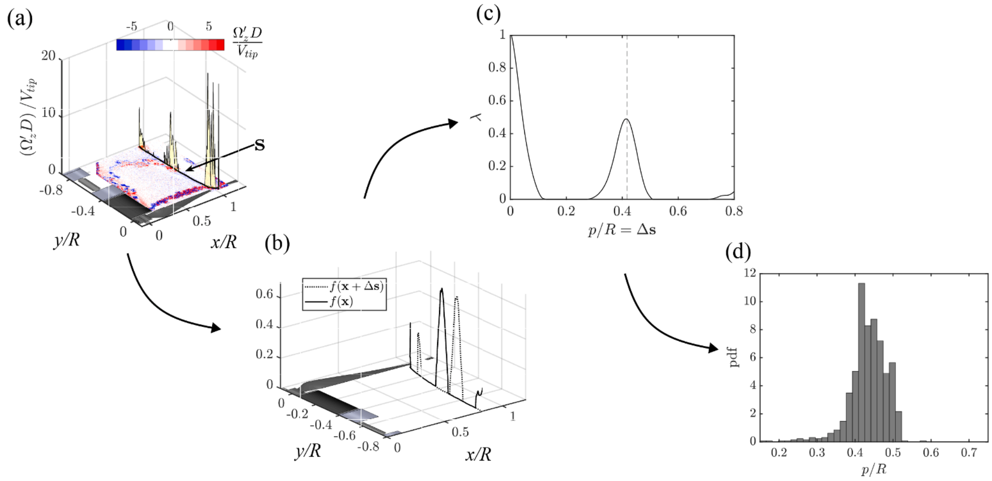

Fig. 4. Schematic representation of the methodology employed for the pitch determination: (a) instantaneous vorticity sampled along the maximum time-averaged vorticity line, (b) illustration of the auto-correlation function, (c) auto-correlation as a function of Δ**s**, (d) probability density function constructed over all the captured snapshots.

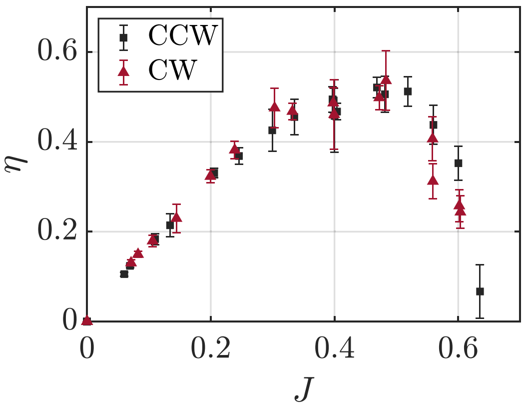

Fig. 5. Propeller efficiency for the CCW and CW cases. The errorbars indicate the estimated uncertainty on η..

to the error propagation of the uncertainties on thrust, torque, and RPM measurements.

Fig. 6 shows the measured thrust ($C_\tau = T/(\rho n^2 D^4)$) and torque ($C_Q = Q/(\rho n^2 D^5)$) coefficients, and the propulsive efficiency η for the CoR configuration, in which both propellers rotate in a counter-clockwise direction.

The results indicate that the interaction between side-by-side propellers leads to a reduction in the thrust and torque coefficients (Fig. 6.a,b). However, the effect on the thrust coefficient is stronger than that on the torque coefficient, leading to a reduction in the propulsive efficiency (Fig. 6.c).

The relative variation due to the propellers' interaction was evaluated as the difference between the coefficients for the CoR and the single propeller case, normalized by the corresponding single propeller case value. This yields three variables: ΔC_τ, ΔC_Q and $\Delta\eta$. For a generic variable χ, the percentage variation can be defined as:

$$\Delta\chi = 100\,\frac{\chi_{CoR} - \chi_{1,Prop}}{\chi_{1,Prop}} \tag{10}$$

Lower advance ratios, corresponding to high loading cases, show a stronger interactions and a wider streamtube upstream the propeller. Fig. 7.a shows that the relative reduction in C_τ is more significant at low advance ratios ($J < 0.2$), as opposed to the torque coefficient, which does not show any appreciable effect of J (see Fig. 7.b). While the specific values at which the performance reduces can be dependent on the specific blade geometry, namely $J < 0.2$, the maximum interaction is still expected at $J = 0$ regardless of the specific case.

Overall, a reduction in the efficiency is found, as it is shown in Fig. 7.c, which can be as large as 4% at $J = 0$.

Averaging over all the evaluated values of J, between 0 and 0.65, the efficiency is reduced by 3.17%, the thrust coefficient by 4.77%, and the torque coefficient by 1.8%. Considering only hovering cases ($J = 0$), the reduction in thrust is in a similar range to the results obtained in [13, 15] (i.e. approximately 8%), which feature similar tip-to-tip clearances.

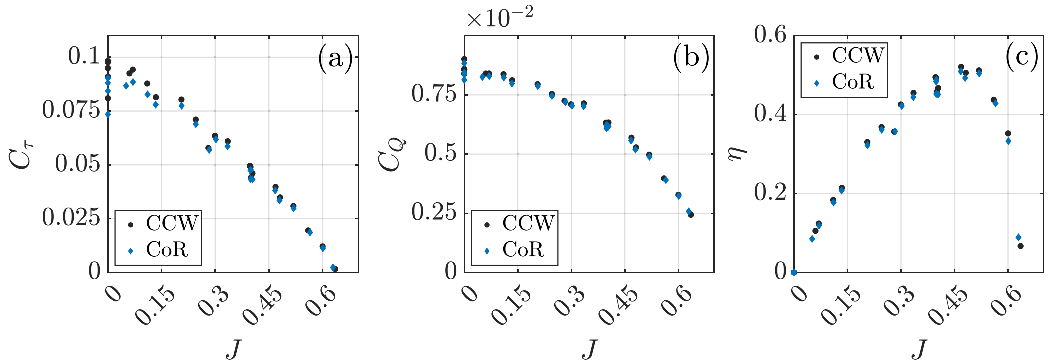

Fig. 6. Performance coefficients at different advance ratios (J) for the single CCW propeller and the two co-rotating CCW propellers cases: (a) thrust coefficient (C_τ); (b) torque coefficient (C_Q) and (c) propeller efficiency (η).

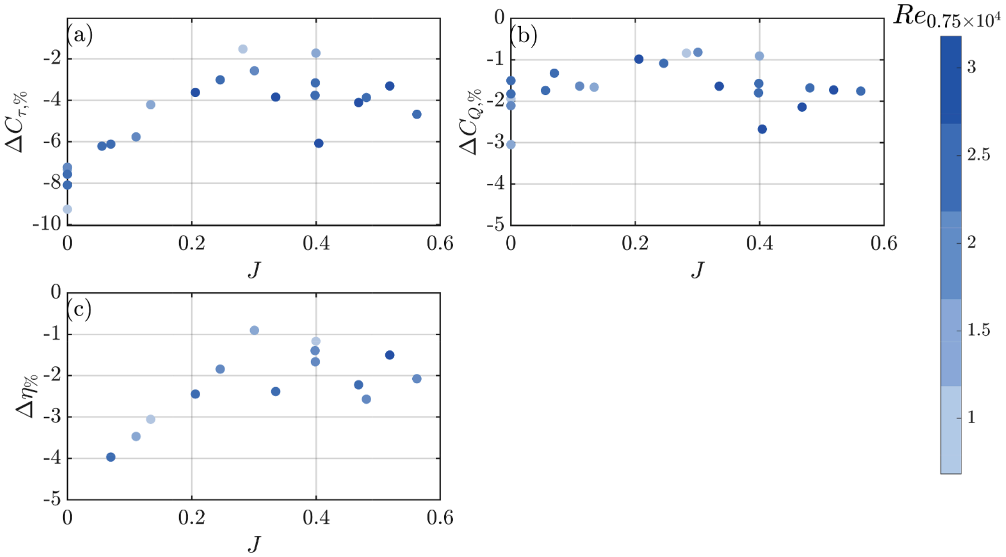

Fig. 7. (a) Relative variation in thrust (C_τ) and (b) torque coefficient (C_Q), and (c) propulsive efficiency (η) due to the aerodynamic interaction at varying advance ratios.

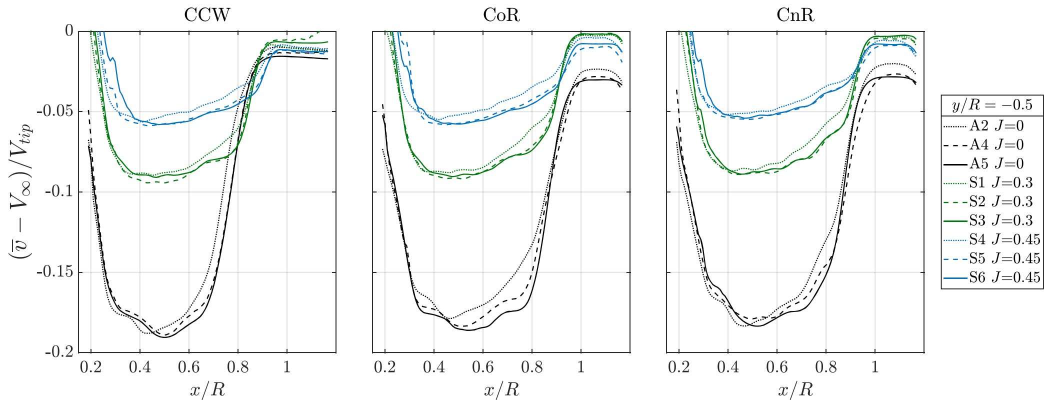

Fig. 8. Normalized streamwise induced velocity profiles along the radial direction (x/R) at $y/R = -0.5$. All cases indicated in Table 2, subplots grouped by operating condition (CCW, CoR and CnR).

The reduction in efficiency for varying J is also in line with similar experiments [1], particularly far from J equal to zero.

3.2. Flow topology

In this section, the time averaged features of the slipstream of the propeller operating in CCW, CoR and CnR conditions will be presented. Here and in the following, v indicates the streamwise velocity, u the radial component and w the azimuthal component.

Fig. 8 shows the streamwise induced velocity profiles ($(\bar{v} - V_\infty)/V_{tip}$) taken at $y/R = -0.5$ for all the investigated cases.

$$V_{tip} = \sqrt{V_\infty^2 + (2\pi nR)^2} \tag{11}$$

The CCW case features greater values of induced velocity, regardless of the specific value of the advance ratio, compared to both the CoR and CnR cases. This difference is the largest at $J = 0$, yet it is still visible at the other values of J. For a fixed value of the advance ratio, the profiles are also collapsing, with only minimum differences that can be attributed to the effect of the different Reynolds numbers. Comparing cases at different values of the advance ratio instead reveals that for the CCW case all the profiles collapse from $x/R > 0.8$. This is not the case when referring to the CoR and CnR cases, where the effect of the interaction with the other propeller modifies the value of the induced velocity, with the greatest deviations observed at $J = 0$.

Further insights into the interaction can be obtained comparing the CCW, CoR and CnR cases, at a fixed value of the RPM. Fig. 9 shows how the streamwise velocity profiles indicate a wider slipstream in the CoR and CnR cases with respect to the CCW case. This effect is stronger at lower advance ratios, while it is almost negligible at $J = 0.45$, and it can be attributed to the mutual induction of the slipstream of the two propellers.

Fig. 10 shows the azimuthal velocity component as a function of the radial coordinate. The profiles are extracted at $y/R = -0.5$ for three values of the advance ratio.

The local peak that can be found at about $x/R = 0.75$ for the CCW case and $J = 0$ is shifted towards the blade tip for the CoR and CnR configurations. This becomes less evident at $J = 0.3$, with instead a practically overlapping azimuthal velocity profile at $J = 0.45$.

In addition to this, comparing the CCW and the CoR case, it can be concluded that the effect of the interaction between the two propellers is such that across the entire disk, the azimuthal velocity reduces at $J = 0$. At greater advance ratios, this difference is progressively attenuated.

Figs. 11 and 12 show the colormaps of the normalized time-averaged radial ($\bar{u}/V_{tip}$) and streamwise ($\bar{v}/V_{tip}$) velocity components, respectively, for the CCW and CoR cases.

From Fig. 11, two considerations can be drawn: firstly, at lower advance ratios, the induced radial velocity is stronger and directed towards the axis of rotation; additionally, $\bar{u}/V_{tip}$ weakens as J increases.

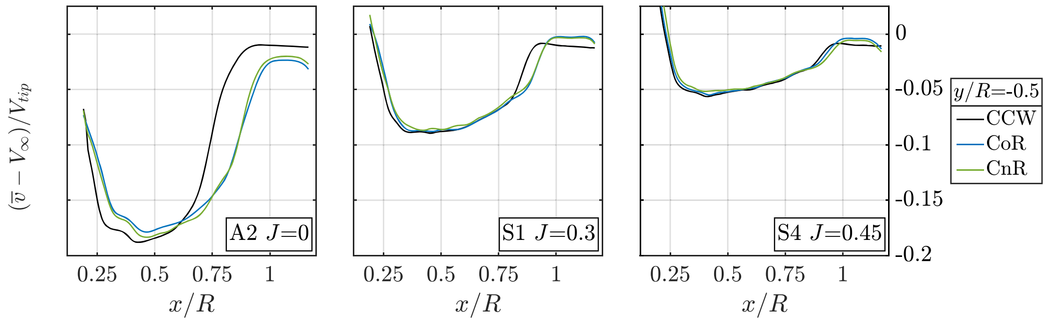

Fig. 9. Normalized streamwise velocity profiles along the radial direction (x/R) at $y/R = -0.5$. Cases at 3000 RPM (A2, S1, and S4), subplots grouped by advance ratio.

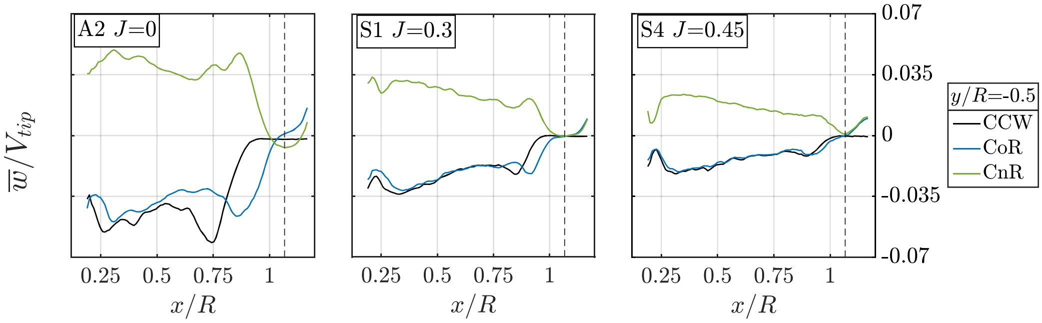

Fig. 10. Normalized azimuthal velocity profiles along the radial direction (x/R) at $y/R = -0.5$. Cases at 3000 RPM (A2, S1, and S4), subplots grouped by advance ratio. The dashed line at $x/R = 1.067$ indicates the midline between the two propellers. .

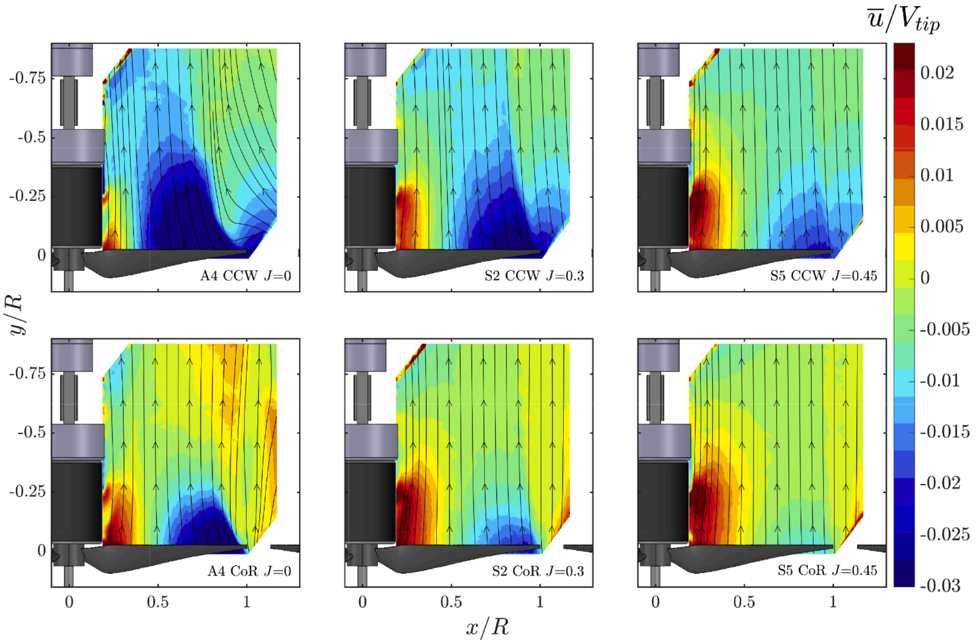

Fig. 11. Colormaps of the normalized radial velocity component measured at 5000 RPM (A4, S2 and S5) and J = 0, 0.3 and 0.45 for CCW and CoR cases.

Secondly, the presence of a second propeller reduces the intensity of the radial velocity component. This is likely because the radial velocities induced by both propellers balance out for the specific measuring plane, as it is also shown in [1].

Focusing on the streamwise component (Fig. 12), case A4 corresponds to the hovering case, where the streamtube can be clearly seen. In addition, the flow progressively accelerates from the propeller blade moving downstream, as it is expected from the momentum theory. At higher values of J there is less difference between the slipstream velocity and the freestream velocity, consistent with the lower disk loading associated with this condition. The propeller slipstreams do not merge in the CoR cases, confirming the findings in [1]. Comparing the CCw and the CoR cases, the slipstream evolution is different, with a wider streamtube in the latter case. To evaluate this, for each case indicated in Table 2, the line of maximum vorticity was taken from the time-averaged vorticity fields, and it was used as an indicator of the edge of the streamtube.

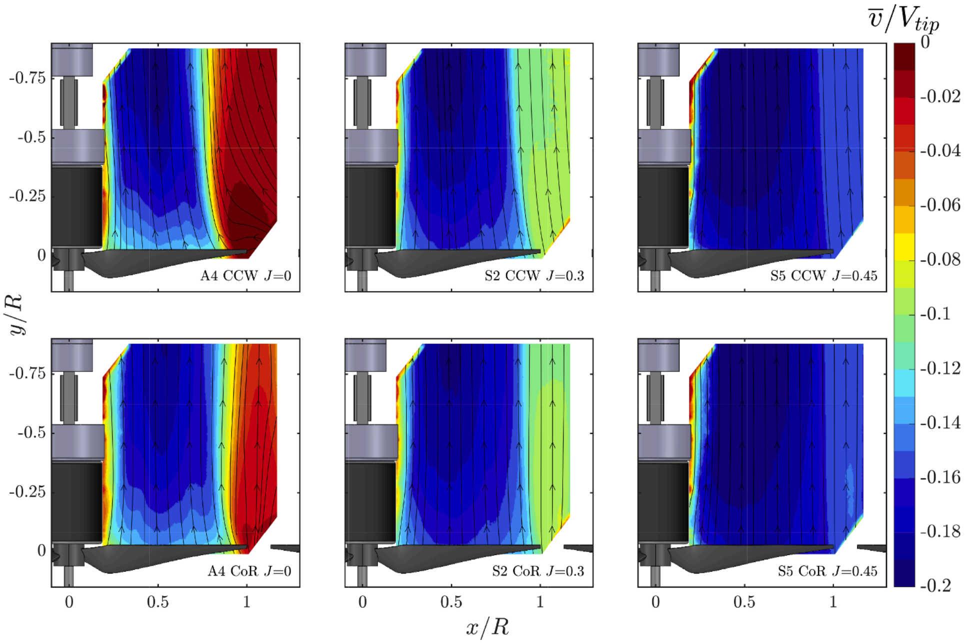

Fig. 12. Colormaps of the normalized streamwise velocity component measured at 5000 RPM (A4, S2 and S5) and J = 0, 0.3 and 0.45 for CCW and CoR cases.

In Fig. 13, the solid line indicates the edge of the streamtube for a single propeller, showing that the width is smaller than the CoR and CnR cases. The effect is stronger at lower advance ratios, and it is equivalent for the CoR and CnR cases. This shows how the rotation direction has a negligible effect on the width of the streamtube and that the interaction is stronger at lower values of J. This observation aligns with the previously reported influence of wake interactions on the thrust and torque.

To further investigate the wake structure, the locations of the tip vortices were identified and superimposed on the streamtube boundaries. The positions of the tip vortices were identified from the phase-averaged vorticity fields obtained with the methodology proposed in Section 2, by applying a threshold to highlight only the regions of the wake characterized by the largest values of vorticity. This threshold was selected for each case, since the vorticity level can vary significantly for different operating conditions. However, it is worth mentioning that it was kept constant across all phases for each condition. The identified connected regions of high vorticity represent the possible vortices. The detection starts from a reference phase, in which the approximate area in which the tip vortices appear is indicated. Within this area, the vortex core is defined as the centroid of the connected region above the threshold. From this starting point, the vortices are then followed automatically through the subsequent phases by selecting, at each step, the region closest to the previously detected position. In this way, the trajectories of the vortices are reconstructed along the wake. The selection of this specific method is driven by its simplicity of implementation and efficiency in the computation. Other approaches were also tested [10,39,40] yet the identification of the vortex location did not differ of values greater than 1% of the vortex radius. As such, the most computationally efficient method was implemented. An example of the vortex tracking results is shown in Fig. 14, where the phase-correlated vorticity $\tilde{\Omega}_z$, normalized by V_{tip}/D, is displayed for six representative phases (out of the 25 considered for the averaging process). The position of the two tracked vortices is marked with green and yellow dots, illustrating their phase evolution. The results confirm that the rotation direction has a negligible effect on the widening of the slipstream on the measured plane, while the interaction between the two propellers plays a dominant role, particularly at low values J.

Effect on the propeller slipstream's pitch

Based on the methodology described in Section 2.3, each vorticity field allowed for the identification of the distance between consecutive tip vortices, with the scope of assessing the effect of the aerodynamic interaction on this parameter. The results regarding the effect of a side-by-side propeller configuration on the slipstream's pitch are shown in Fig. 15 in the form of bar charts of the percentage variation of the pitch with respect to the CCW case. The hovering cases (A2, A4, and A6 in Table 2) show an increase in pitch due to the propellers' interaction. The slipstream of an isolated propeller at $J = 0$ is the most turbulent condition owing to the interaction between consecutive vortices in the absence of a mean flow. The increased pitch in the twin-propeller configuration suggests that the interaction of the two slipstreams can have a stabilizing effect on the evolution of the tip vortices, leading to a less turbulent wake. This will be addressed in the next section.

It is worth mentioning that at low values of J, the less ordered structure of the wake leads to an early coalescence of the tip vortices, which can affect the results of the auto-correlation. This is the same reason for which in Fig. 13 no vortices are recognized downstream of $y/R = -0.5$. At $J > 0$, it is interesting to highlight the effect of the two propellers operating at the same time, which in turn leads to a reduction in the effective pitch of about 10% compared to the single propeller case.

Phase-resolved analysis

This section analyses the turbulent kinetic energy and phase-correlated kinetic energy, defined in Section 2 based on the triple decomposition of the velocity fields.

Phase-resolved reconstructions were carried out for all the tested configurations. However, a fundamental distinction must be made in the interpretation of the results for each scenario. For the single propeller cases, phase averaging is straightforward, as is the analysis of the wake flow fields, since the entire flow field is influenced by a single periodic forcing. In contrast, for the twin propeller configurations, phase averaging is only applied according to the propeller whose blade is fully visible in the field of view. As a result, the wake structures associated with this propeller can still be meaningfully reconstructed across different phases. However, the second propeller introduces an additional

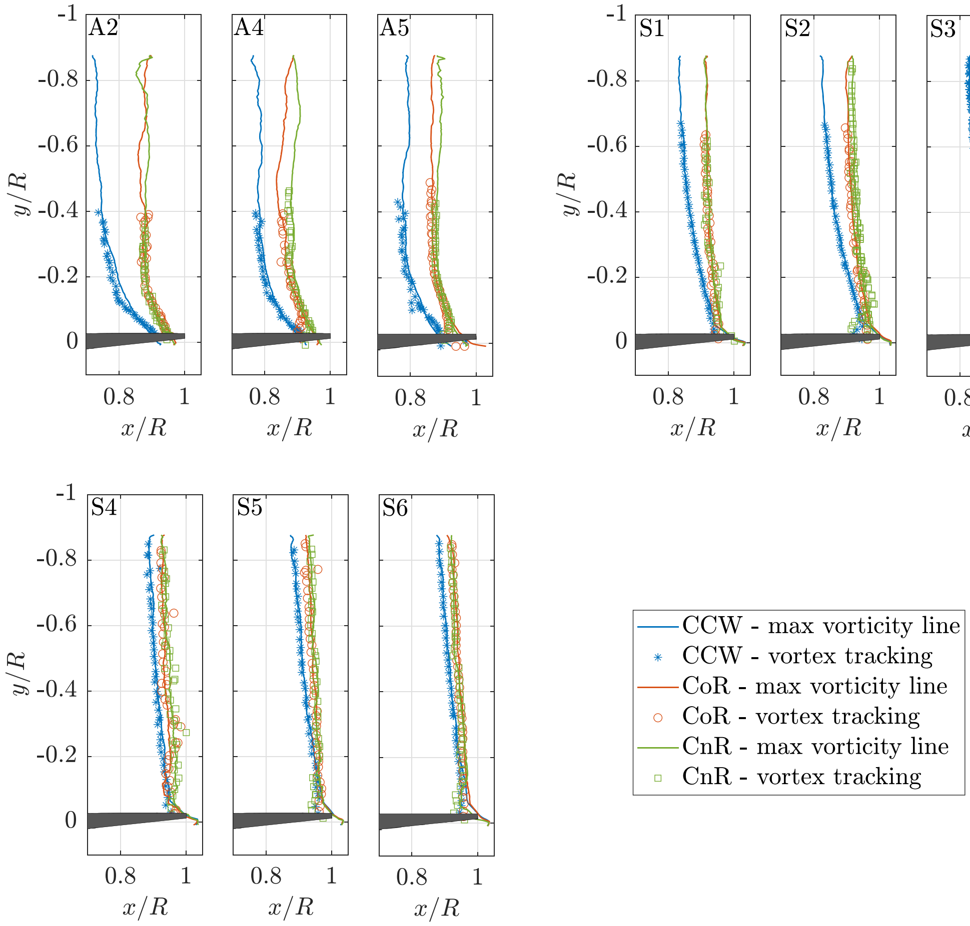

Fig. 13. Traces of the maximum time-averaged vorticity, describing the edge of the streamtube. For each case, the CCW, CoR and CnR cases are compared. The markers indicate the location of the vortex cores detected from the phase-averaged vorticity fields..

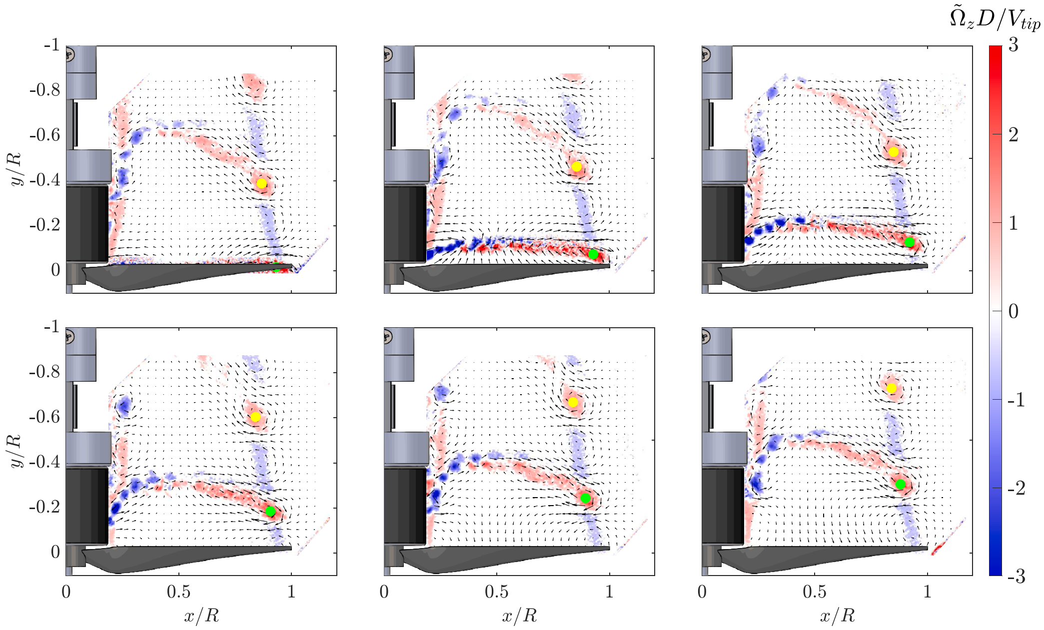

Fig. 14. Out of plane phase - correlated vorticity $\tilde{\Omega}_z$ for a single propeller case, operating at 3000 RPM and $J = 0.3$, normalized by V_{tip}/D, for six different ordered phases. Yellow and green dots track the location of tip vortices along the wake. For clarity, quiver vectors are subsampled and only one every ten is displayed.. (For interpretation of the references to colour in this figure legend, the reader is referred to the web version of this article.)

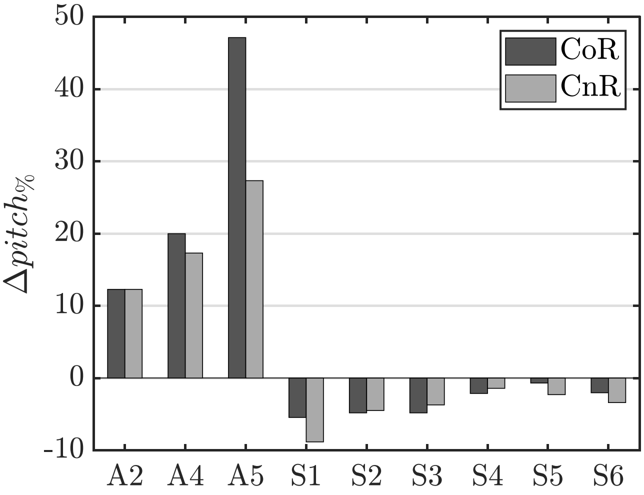

Fig. 15. Relative variation in pitch for CoR and CnR configurations.

random disturbance owing to the lack of synchronization between the two propellers.

Due to this limitation, the analysis of TKE and PKE across different phases and different advance ratios is performed only for the single propeller configuration, where phase coherence is fully preserved. Nevertheless, a comparative study of the TKE through the different configurations (single propeller and twin propellers) is carried out to assess how the presence of a second propeller affects the turbulence distribution. In this case, the second propeller acts as a random disturbance.

For the sake of conciseness, and without leading the generality of the discussion, only the results obtained at 3000 RPM are reported.

Figs. 16 and 17 show the effect of the advance ratio on the TKE and PKE fields, respectively, in the CCW case. Specifically, phase-averaged fields are extracted for three representative and progressive phases. It can be observed that both TKE and PKE decrease as the vortex evolves downstream (i.e. as it moves toward increasingly negative values of y/R, from phase a to phase c). This indicates that the turbulent energy is highest near the propeller and subsequently dissipates as the flow evolves downstream. Additionally, the PKE and TKE distributions appear less coherent and more diffused for lower advance ratios, while they become increasingly localized around the vortices as J increases. This suggests that, consistently with the general picture of a less organized wake at $J = 0$, the turbulence is more coherent and concentrated within the vortex cores closer to the optimal operating condition, whereas, at lower advance ratios, it is more dispersed throughout the wake.

Fig. 18 investigates the impact of different propeller configurations at a fixed operating condition of 3000 RPM and $J = 0.3$. Three representative phases indicated with a, b and c are shown. By focusing on the central region of the wake, it is possible to assess how the TKE field of the investigated propeller is affected by the presence of the second propeller, which acts as a quasi-random external forcing. In Fig. 18, the three different operating conditions, namely, CCW, CoR and CnR, are indicated with the numbers 1, 2 and 3. The results suggest that the TKE attains lower values in the presence of two propellers compared to the single-propeller case. Furthermore, the reduction in the TKE ap-

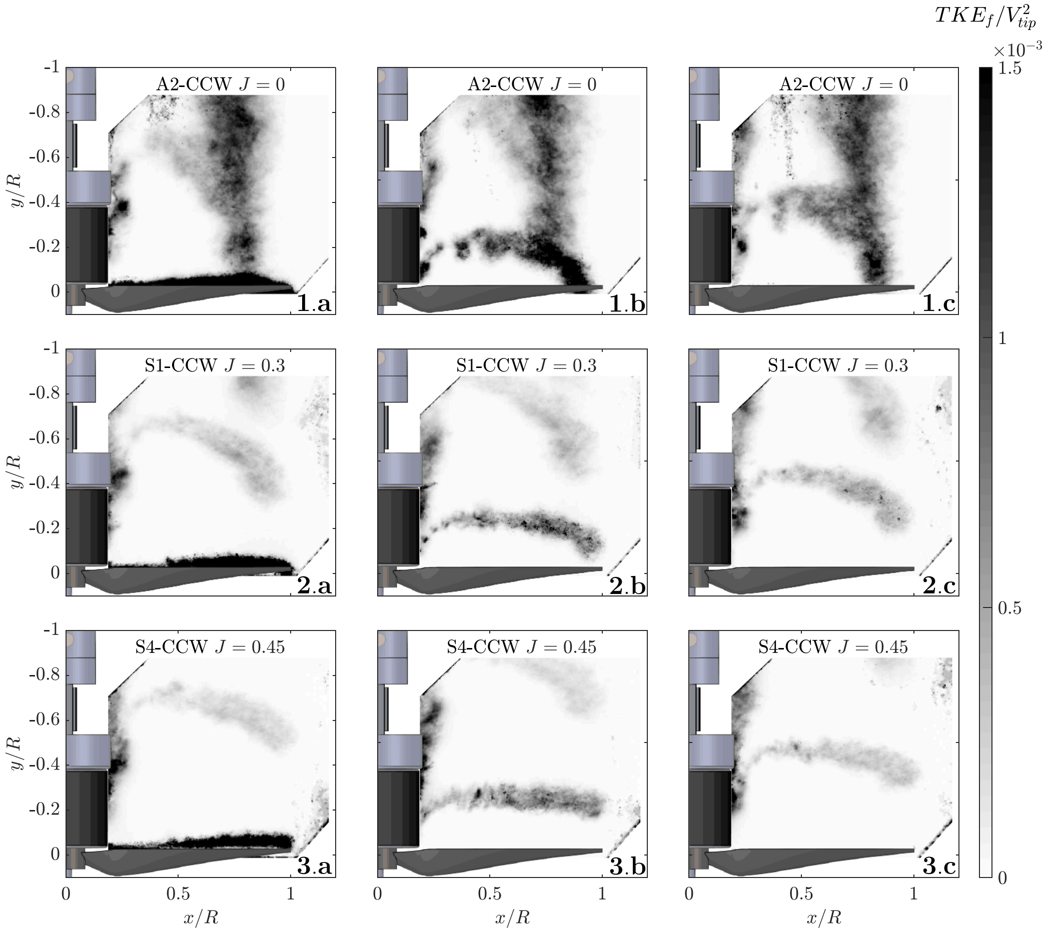

Fig. 16. Effect of the advance ratio ($J = 0$, 0.3 and 0.45) on the TKE, considering the single propeller case configuration, with the propeller operating at 3000 RPM. For each advance ratio three phases are considered (from a to c).

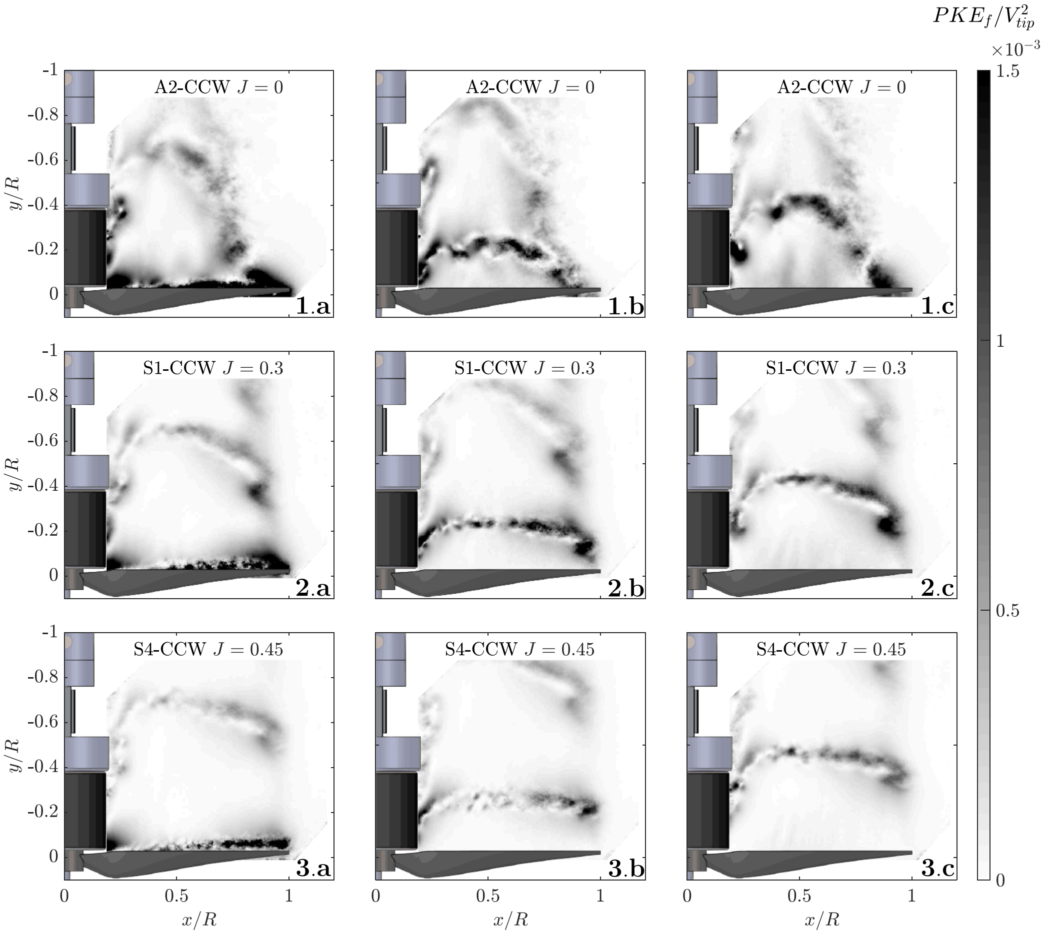

Fig. 17. Effect of the advance ratio ($J = 0$, 0.3 and 0.45) on the PKE, considering the single propeller case configuration, with the propeller operating at 3000 RPM. For each advance ratio, three phases are considered (from a to c).

pears more significant for the counter-rotating propeller configuration compared to the co-rotating case. To support this observation, a quantitative evaluation was carried out by restricting the analysis to the central region of the wake, highlighted in red in Fig. 18. This region was selected both because it represents the portion of the flow where the wake dynamics are most relevant for the comparison, and because the outer regions are those most affected by spurious reflections. For each configuration (CCW, CoR and CnR) and for each phase f, the TKE field was spatially averaged within this region, and the resulting values were then averaged over all 25 phases, yielding for each case a value defined as $\overline{TKE} = \sum_{f=1}^{N_{\text{phases}}} TKE_f$. The relative variation of TKE with respect to the single-propeller case was computed as

$$\Delta TKE_{\text{CoR, CnR}} = 100\,\frac{\overline{TKE}_{\text{CoR, CnR}} - \overline{TKE}_{\text{CCW}}}{\overline{TKE}_{\text{CCW}}} \tag{12}$$

This analysis leads to values of $\Delta TKE_{\text{CoR}} = -13.3\%$ and $\Delta TKE_{\text{CnR}} = -16.5\%$, in agreement with the qualitative trends discussed above.

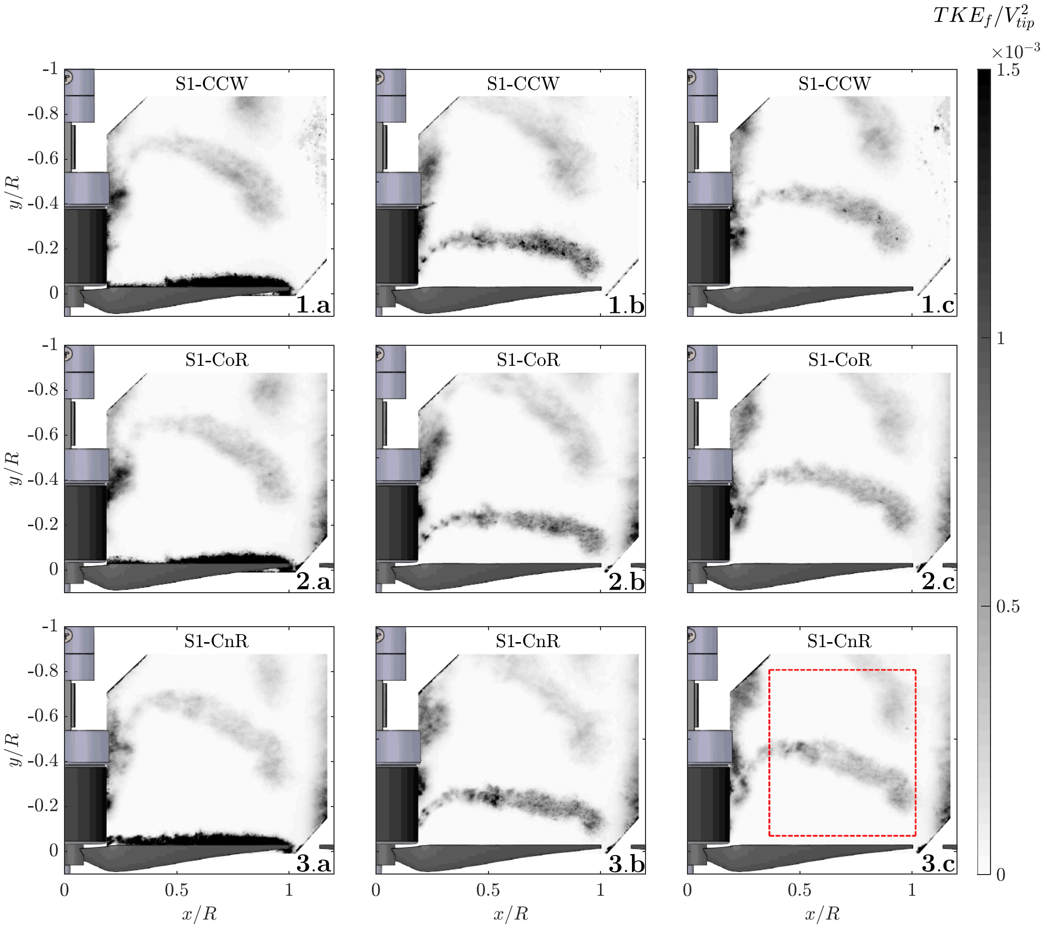

Fig. 18. Impact of different propeller configurations (CCW, CoR and CnR) on the TKE, considering propellers operating at a fixed condition of 3000 RPM and $J = 0.3$. For each configuration, three phases are considered (from *a* to *c*). In subfigure 3*c*, the red dashed rectangle highlights the central wake region, which was later used for the quantitative analysis discussed in the text.. (For interpretation of the references to colour in this figure legend, the reader is referred to the web version of this article.)

4. Conclusions

In this paper, the aerodynamic interaction of two small propellers positioned in a side-by-side arrangement and with the rotational axis aligned to the freestream was experimentally investigated. The primary objectives were to assess the effects of aerodynamic interaction on the performance and discern the changes in the flow topology, focusing on the modification of the evolution of the tip vortex and the turbulence properties of the wake.

The thrust and torque of one of the two propellers were measured for several advance ratios both in the isolated case and when both propellers were operated at the same time. Tests were performed comparing the performance of a single propeller with that generated in a co-rotating and counter-rotating arrangement.

The results indicate that, averaging over all the cases tested, ranging from $J = 0$ to $J = 0.65$, the effects of the interaction are a 4.77% and 1.8% average reduction in the thrust and torque coefficient, respectively, which leads to a 3.2% reduction in the efficiency of the propeller. The effect depends on the advance ratio (J), as it was noted that lower values of J are associated with greater changes in the performance parameters.

The characteristics of the wake's flow field structure were studied through stereoscopic particle image velocimetry at three different advance ratios representing hovering ($J = 0$), a high loading case in forward flight ($J = 0.3$) and a condition close to maximum efficiency ($J = 0.45$).

When operating in a twin-propeller arrangement, the slipstream widens, with a corresponding reduction of the streamtube upstream the propeller. The most affected conditions are those characterized by a low value of the advance ratio, which correspond to cases where the streamtube would be the largest. This interaction leads to a loss of performance, as measured with the load and torque cells.

The flow statistics are also significantly affected by the interaction. The radial and the aximuthal velocity components are reduced in the CoR and CnR cases compared to the CCW case, with little dependence on the direction of the rotation. In addition to this, the streamwise velocity is also affected, with a reduced shear layer at the interface between the two slipstream.

The mean distance between two consecutive vortices, which is referred to as pitch in the present manuscript, is significantly affected by the operating conditions. In particular, at $J = 0$ the pitch increases with respect to the isolated case of values as large as 30%. This suggests an attenuation in the wake turbulence, owing to a reduced interaction between the tip vortices that typically yields a less ordered structure of the wake in hover conditions. On the other hand, at J equal to 0.3 and 0.45, a reduction of less than 10% was evaluated, meaning that the vortical structures are closer together in this case.

A triple decomposition of the phase-averaged velocity field was carried out, highlighting that when the propeller is working far from its design point, higher turbulence levels are found in the wake. Conversely, the effect of the second propeller is such that it attenuates the turbulence intensity, a 13.3% and 16.5% reduction in the turbulent kinetic energy was evaluated for the CoR and CnR configurations, respectively, at $J = 0.3$.

The presented study discusses the aerodynamic interaction of side-by-side propellers operating at low Reynolds numbers. However, the discussion is limited to a fixed geometry in terms of the propeller's size, the blade twist and chord distribution, and the spacing between the rotation axes. Nevertheless, the physical mechanisms driving the interaction are not related to the blade geometry, and similar interaction effects and trends should be expected in similar configurations, as also encountered by previous studies.

Future work will focus on the effect of the Reynolds number and the propeller geometry of side-by-side configurations, as it has been well established in the literature that the maximum interaction is obtained at the minimum spacing. The effect of the number of blades could also be explored, as including the rotor solidity as a test parameter allows for studying the effect of blade loading at equal thrust settings, for instance.

CRediT authorship contribution statement

Paolo Comunian: Writing – review & editing, Writing – original draft, Methodology, Investigation, Formal analysis, Data curation, Conceptualization; **Sara Montagner:** Writing – review & editing, Writing – original draft, Methodology, Investigation, Formal analysis, Data curation, Conceptualization; **Jacopo Serpieri:** Writing – review & editing, Supervision, Methodology, Formal analysis, Data curation, Conceptualization; **Gioacchino Cafiero:** Writing – review & editing, Supervision, Methodology, Funding acquisition, Formal analysis, Data curation, Conceptualization.

Data availability

Data will be made available on request.

Declaration of competing interest

The authors declare the following financial interests/personal relationships which may be considered as potential competing interests: Paolo Comunian reports financial support was provided by MOST Centro Nazionale per la Mobilità Sostenibile. If there are other authors, they declare that they have no known competing financial interests or personal relationships that could have appeared to influence the work reported in this paper.

Acknowledgment

This study was carried out within the MOST – Sustainable Mobility National Research Center and received funding from the European Union Next-GenerationEU (PIANO NAZIONALE DI RIPRESA E RESILIENZA (PNRR) – MISSIONE 4 COMPONENTE 2, INVESTIMENTO 1.4 – D.D. 1033 17/06/2022, CN00000023). This manuscript reflects only the authors' views and opinions, neither the European Union nor the European Commission can be considered responsible for them.

SM was supported by a scholarship funded through the WINDED Scalability Project, (PIANO NAZIONALE DI RIPRESA E RESILIENZA (PNRR) – MISSIONE 4 COMPONENTE 2, INVESTIMENTO 1.4 – D.D. 1033 17/06/2022, CN00000023).

The authors wish to thank Alessandro Sanginario for contributing to the fabrication of the 3D-printed propellers.

References

[1] R. Vries, N.V. Arnhem, T. Sinnige, R. Vos, L.L. Veldhuis, Aerodynamic interaction between propellers of a distributed-propulsion system in forward flight, Aerosp. Sci. Technol. 118 (2021) 107009.

[2] P. Comunian, J. Serpieri, G. Cafiero, A genetic-algorithm based approach for optimized distributed propulsion, in: AIAA AVIATION FORUM AND ASCEND 2024, 2024, p. 3603.

[3] P. Comunian, J. Serpieri, G. Cafiero, A Numerical Framework for Multiparametric Optimization of Distributed Electric Propulsion, J. Aircr. (2025).

[4] F.D. Gregorio, K. Rossignol, G. Ceglia, J. Yin, Aerodynamic and acoustic interactional effects for small commercial propellers in co-axial counter-rotating arrangements, Aerosp. Sci. Technol. 159 (2025) 110001.

[5] T.J. Mueller, J.D. Delaurier, Aerodynamics of small vehicles, Annu. Rev. Fluid Mech. 35 (1) (2003) 89–111.

[6] E. Grande, D. Ragni, F. Avallone, D. Casalino, Laminar separation bubble noise on a propeller operating at low Reynolds numbers, AIAA J. 60 (9) (2022) 5324–5335.

[7] D. Casalino, E. Grande, G. Romani, D. Ragni, F. Avallone, Definition of a benchmark for low Reynolds number propeller aeroacoustics, Aerosp. Sci. Technol. 113 (2021) 106707.

[8] G. Capobianchi, S. Montagner, A. Piccolo, A. Di, F. Marco, G. Avallone, D. Cafiero, E. Ragni, L.G.D. Paola, Stoica, Impact of turbulent inflow on the far-field noise generated by a propeller operating at low Reynolds number, in: th AIAA/CEAS Aeroacoustics Conference, 2024, p. 3154.

[9] A. Grava, J. Serpieri, L. Bernardos, G. Cafiero, Multi-fidelity analysis of a small-scale propeller using vpm against urans and experimental data, in: AIAA AVIATION FORUM and ASCEND 2025, 2025, p. 3163.

[10] A. Grava, J. Serpieri, G. Iuso, L. Bernardos, G. Cafiero, Experimental investigation of a small drone propeller aerodynamics in forward flight, 2024, pp. 1–12.

[11] L.L. Veldhuis, M. Kotsonis, E.V. Berkel, Non-uniform inflow effects on propeller performance, in: 31st AIAA Applied Aerodynamics Conference, 2013, p. 2801.

[12] T.C. Stokkermans, D. Usai, T. Sinnige, L.L. Veldhuis, Aerodynamic interaction effects between propellers in typical evtol vehicle configurations, J. Aircr. 58 (4) (2021) 815–833.

[13] W. Zhou, Z. Ning, H. Li, H. Hu, An experimental investigation on rotor-to-rotor interactions of small uav propellers, in: 35th AIAA Applied Aerodynamics Conference, 2017, p. 3744.

[14] F.D. Gregorio, P. Candeloro, G. Ceglia, T. Pagliaroli, 2802, IOP Publishing, 2024.

[15] R.E. Nargi, P. Candeloro, F.D. Gregorio, G. Ceglia, T. Pagliaroli, Fluid-dynamic and aeroacoustic characterization of side-by-side rotor interaction, Aerospace 10 (10) (2023) 851.

[16] A. Zanotti, D. Algarotti, Aerodynamic interaction between tandem overlapping propellers in evtol airplane mode flight condition, Aerosp. Sci. Technol. 124 (2022) 107518.

[17] E.D. Paola, R. Camussi, L.G. Stoica, A. Di, G. Marco, Capobianchi, Aerodynamic and aeroacustic experimental investigation of a three propellers dep configuration, Available at SSRN 4858399, 2024.

[18] K.A. Pascioni, S.A. Rizzi, N. Schiller, Noise reduction potential of phase control for distributed propulsion vehicles, in: AIAA Scitech 2019 Forum, 2019, p. 1069.

[19] F.D. Duchetto, T. Pagliaroli, P. Candeloro, K.-S. Rossignol, J. Yin, Aeroacoustic study of synchronized rotors, Aerospace 12 (2) (2025) 162.

[20] E. Amico, S. Montagner, J. Serpieri, G. Cafiero, An a posteriori data-driven method for phase-averaging optical measurements, Meas. Sci. Technol. 2025.

[21] S. Lee, S. Chae, S.Y. Woo, J. Jang, J. Kim, Effects of rotor-rotor interaction on the wake structure and thrust generation of a quadrotor unmanned aerial vehicle, IEEE Access 9 (2021) 85995–86016.

[22] A. Piccolo, R. Zamponi, F. Avallone, D. Ragni, Modification of amiet's model for turbulence-ingestion noise prediction in rotors, J. Acoust. Soc. Am. 158 (1) (2025) 461–475.

[23] P. Candeloro, D. Ragni, T. Pagliaroli, Experimental investigation on the application of serrated trailing edge propellers for drone noise reduction, Appl. Acoust. 242 (2026) 111045.

[24] G. Romani, E. Grande, F. Avallone, D. Ragni, D. Casalino, Performance and noise prediction of low-Reynolds number propellers using the lattice-boltzmann method, Aerosp. Sci. Technol. 125 (2022) 107086.

[25] M. Alì, A. Piccolo, R. Zamponi, D. Ragni, F. Avallone, On the impact of turbulent inflow on the noise generated by a propeller operating at low Reynolds number, 2025.

[26] M. Picillo, M. Barbarino, F. Avallone, Mid-fidelity framework for rotor noise prediction in maneuvering flight, 2025.

[27] A. Grava, J. Serpieri, G. Iuso, L. Bernardos, G. Cafiero, Experimental investigation of a small drone propeller aerodynamics in forward flight, AIAA J. 63 (5) (2025) 1855–1866.

[28] C. Willert, Stereoscopic digital particle image velocimetry for application in wind tunnel flows, Meas. Sci. Technol. 8 (12) (1997) 1465.

[29] A.K. Prasad, Stereoscopic particle image velocimetry, Exp. Fluids 29 (2) (2000) 103–116.

[30] R. Tsai, A versatile camera calibration technique for high-accuracy 3d machine vision metrology using off-the-shelf tv cameras and lenses, IEEE J. Rob. Autom. 3 (4) (1987) 323–344.

[31] B. Wieneke, Volume self-calibration for 3d particle image velocimetry, Exp. Fluids 45 (4) (2008) 549–556.

[32] M. Raffel, C. Willert, S. Wereley, J. Kompenhans, Particle Image Velocimetry: A Practical Guide, 2007.

[33] S. Adatrao, A. Sciacchitano, Elimination of unsteady background reflections in PIV images by anisotropic diffusion, Meas. Sci. Technol. 30 (3) (2019) 035204.

[34] T. Astarita, G. Paolillo, et al, PaIRS: a free software application for robust and accurate digital particle image velocimetry, 2022.

[35] J. Tenenbaum, V. Silva, J. Langford, A global geometric framework for nonlinear dimensionality reduction, Science 290 (5500) (2000) 2319–2323.

[36] P. Baj, P.J. Bruce, O.R. Buxton, The triple decomposition of a fluctuating velocity field in a multiscale flow, Phys. Fluids 27 (7) (2015).

[37] C.S. Greco, G. Cardone, J. Soria, On the behaviour of impinging zero-net-mass-flux jets, J. Fluid Mech. 810 (2017) 25–59.

[38] T. Sinnige, R.D. Vries, B.D. Corte, F. Avallone, D. Ragni, G. Eitelberg, L.L. Veldhuis, Unsteady pylon loading caused by propeller-slipstream impingement for tip-mounted propellers, J. Aircr. 55 (4) (2018) 1605–1618.
[39] L. Graftieaux, M. Michard, N. Grosjean, Combining PIV, POD and vortex identification algorithms for the study of unsteady turbulent swirling flows, Meas. Sci. Technol. 12 (9) (2001) 1422.
[40] M. Zaccara, G. Paolillo, G. Cafiero, T. Astarita, G. Iuso, G. Cardone, C.S. Greco, Near field evolution of wingtip vortices under synthetic-jet based control, Aerosp. Sci. Technol. 148 (2024) 109068.